Chapter 14
Generating Magnetic Fields for Controlling Nanorobots in Medical Applications

Simone Schürle, Bradley E. Kratochvil, Salvador Pané, Mohammad Arif Zeeshan, and Bradley J. Nelson

Abstract During the past decade, significant progress has been shown in nanoscale drug delivery systems, systems for in vitro-testing such as lab-on-chip devices, endoscopic capsules, and robotics for minimally invasive medicine. Advances in nanofabrication technology yielded many new approaches for the batch fabrication process of nanoscale drug carriers including nanotubes, nanowires, and nanoparticles. A major issue is the powering and steering control of these untethered devices in order to allow in vivo interaction with the human body. Several approaches have been suggested that can be categorized as energy storage, energy harvesting, and energy transmission. One promising technique in the class of power transmission is magnetism. Magnetic forces and torques can be applied directly to magnetic material and enable navigation in bodily fluids. In this chapter, we focus on wireless magnetic control of nano drug delivery systems and, in particular, the generation of the required magnetic fields.

14.1 Introduction

Micro- and nanorobots have the potential to revolutionize many aspects of medicine. These untethered, wireless controlled and powered devices will make existing therapeutic and diagnostic procedures less invasive and will enable new procedures never before possible. Miniaturization of functional devices down to nanoscale dimensions has been enabled through the advancement and new development of both bottom up and top down approaches in nanotechnology. This paves the way for many life science applications such as in vitro molecular diagnosis and

S. Schürle • B.E. Kratochvil • S. Pané • M.A. Zeeshan • B.J. Nelson (✉)
Institute of Robotics and Intelligent Systems, CLA H 17.1, Tannenstrasse 3, 8092 ETH Zurich, Switzerland
e-mail: schuesim@ethz.ch; kratochvil@iris.mavt.ethz.ch; vidalp@ethz.ch; marifzee@ethz.ch; bnelson@ethz.ch

C. Mavroidis and A. Ferreira (eds.), *Nanorobotics: Current Approaches and Techniques*, DOI 10.1007/978-1-4614-2119-1_14,

biochemical analysis as well as in vivo interaction with the human body [1]. However, when scaling down the physics that predominates changes, for example, imagine a microrobot in the circulatory system. The fluid dynamics change and inertia becomes irrelevant. Instead surface forces that result in significant viscous drag dominate.

A major point to consider is powering the devices. Powering techniques can be classified into three main categories: onboard, scavenged, and transmitted power [2]. Although batteries offer an inexpensive power source, they are not promising candidates since the total deliverable energy scales with volume. Microelectromechanical system (MEMS)-based power generators provide higher energy densities and several approaches to convert various types of energy into electrical energy have been proposed [3, 4]. A desirable way for powering would be to harvest chemical energy directly from the environment such as biofuel cells. Alternatively, power can be instead transmitted wirelessly.

One approach to wireless transmission is the use of magnetic fields. Here it can be further distinguished by induction or by direct application of magnetic forces and torques. From a medical point of view, the magnetic permeability of the human body is approximately the same as that of air, so there are no significant interactions of tissue with low-frequency magnetic fields, as opposed to electric fields. The basic principle of transmitting electrical power with magnetic fields is based on Faraday's law of induction. When current flows in a circuit (primary), a magnetic field is generated in its surroundings. An effective voltage source develops in any nearby circuit (secondary) [5]. Many mesoscale devices incorporate this principle [6–8]. Large coils outside the body generate a varying field that is captured by small coils embedded in capsules. However, at the microscale the challenge is in designing the receiver coils, because they are constrained by planar microfabrication processes. Additionally, the efficiency of voltage rectification on the receiver side becomes increasingly important as the device scales down because the induced voltage amplitude decreases as well.

For microrobots made of a ferromagnetic material, energy can be transmitted directly by an externally applied magnetic field. A magnetic body subjected to an external magnetic field will experience a torque related to the field strength and the magnitude of its own magnetization as well as a magnetic force that is related to the field gradient and the body's magnetization and volume [9].

There is a large body of work describing different possible drug carriers based on magnetic nanospheres or nanowires and nanotubes that are manipulated by externally applied magnetic fields. Ideas to combine these manipulation methods with existent MRI technology have been proposed [10].

In this chapter, we discuss the approach and theory of direct magnetic manipulation of magnetic nanomaterial and explain in detail a system for generating fields for 5-DOF control of nonspherical magnetic bodies. We also give a brief review of current batch fabrication methods of magnetic nanoagents suitable for in vivo medical applications.

14.2 Manipulation of Magnetic Bodies in Fluids

14.2.1 Swimming Behavior at Low Reynolds Numbers

Consider an object of characteristic dimension a which is moving through a liquid at velocity ϑ. The viscosity of the fluid is expressed by η and the density by ρ. Introduced by Osborne Reynolds, the ratio of the inertial force to the viscous force is called the Reynolds number and can be expressed as

$$\mathrm{Re} = \frac{a\vartheta\rho}{\eta} \text{ or } \mathrm{Re} = \frac{a\vartheta}{\nu}, \tag{14.1}$$

where ν is the kinematic viscosity of the fluid. From the equation we can understand that for low Re we are in a world that is either very viscous, very slow, or very small. Low Re flow around a body is referred to as creeping flow or Stokes flow. Further, the flow pattern does not change appreciably whether it is slow or fast, and the flow is effectively reversible. Consequently, reciprocal motion results in negligible net movement [11].

For a better understanding of how different physics are in this world of low Re, consider the locomotion principles of microorganisms in nature. We distinguish between three different basic methodologies of how microorganisms swim [12, 13], as illustrated in Fig. 14.1. For example, cilia are active organelles that are held perpendicular to the flow during the power stroke and parallel to the flow during the recovery stroke. Many cilia are used simultaneously. Another kind of active organelles are eukaryotic flagella. They deform to create paddling motions, such as traveling waves or circular translating movements. Bacterial (prokaryotic) flagella work differently and use instead a molecular motor to turn the base of a passive flagellum [11].

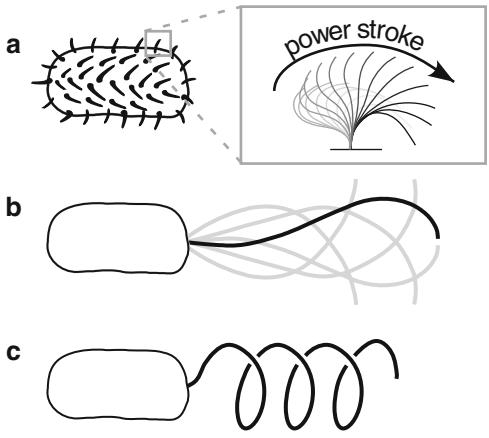

Fig. 14.1 *Locomotion of microorganisms*. (**a**) Cilia move across the flow during the power stroke, and fold near the body during the recovery stroke. (**b**) Eukaryotic flagella create patterns such as traveling waves. (**c**) A molecular motor spins a passive bacterial flagella (reprinted with permission from [11])

A number of bio-inspired robotic swimming methods have been published that try to mimic the locomotion principle for an effective way of transportation. However, many of these techniques require mechatronic components that present challenges in microfabrication and wireless power and control [14, 15]. Almost all these methods use magnetic fields. As discussed above, this actuation principle is attractive since no other method offers the ability to transfer such large amounts of power wirelessly over relatively large distances. Also, a variety of control strategies have been proposed for navigating wireless microrobots such as gradient magnetic fields, stick–slip actuation based on rocking magnetic fields, or by exploiting resonating structures. Bio-inspired magnetically driven propulsion techniques of helical shaped microagents that mimic a bacteria flagellum have been suggested. A rotating magnetic field can be used to rotate a helical propeller [16, 17], eliminating the need to replicate a molecular motor in a microrobot.

A controllable external pulling source is not available for microorganisms; however, we can generate such a source and utilize gradients in magnetic fields to apply forces and torques directly on untethered microrobots; a strategy that obviously could not have evolved through natural selection.

14.2.2 Modeling the Magnetization of Soft Magnetic Bodies

Direct-gradient propulsion is a noncontact manipulation method that can be realized by the use of either permanent or soft magnetic materials. In the first case, the magnetization of the object does effectively not depend on the applied magnetic field, and the object can be modeled as a simple magnetic dipole. The resulting equations for the torque and the force acting on the object are easily determined [18].

If we consider a soft magnetic material, we face easier fabrication methods as well as different issues in control. Additionally, soft magnetic materials can reach levels of magnetization as high as the remanence magnetization of permanent magnets [4, 19, 20]. However, with soft magnetic materials, the magnetization of the body is a nonlinear function of the applied magnetic field. Hence, the relationship between the applied field and the resulting torque and force is nontrivial [18].

The control of soft magnetic beads has been studied widely [10, 21, 22]. Here, a spherical shape simplifies the control problem since there is no preferred direction of magnetization. However, let us now consider a soft magnetic body with a unique axis of symmetry, as shown in Fig. 14.2. We choose ellipsoids as it has been shown that many simple geometries can be accurately modeled magnetically as ellipsoids [23, 24]. Regarding the shape of nanowires as potential drug carriers, we then model the magnetization of a cylindrical body based on its ellipsoidal equivalent.

As illustrated in Fig. 14.2, the body coordinate frame is located at the center of mass and the x-axis is aligned with the axis of symmetry. The body is magnetized to a magnetization $\mathbf{M}$ in units ampere per meter (A/m) by an external magnetic field $\mathbf{H}$ (A/m) at the body's center of mass. Because of the symmetry of the body, the field $\mathbf{H}$, the magnetization $\mathbf{M}$, and the axis of symmetry are coplanar. The applied magnetic field can be also expressed as an applied magnetic flux density $\mathbf{B}$ with the

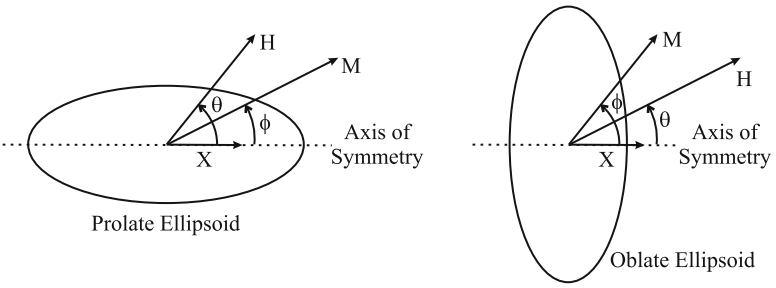

Fig. 14.2 *Axially symmetric bodies in an external magnetic field*. The x-axis of the body frame is aligned with the axis of symmetry. The field $\mathbf{H}$, the magnetization $\mathbf{M}$, and the axis of symmetry are coplanar. $\theta \in [0°, 90°]$ is the angle between $\mathbf{H}$ and the axis of symmetry, and $\varphi \in [0°, 90°]$ is the angle between $\mathbf{M}$ and the axis of symmetry (reprinted with permission from [18])

unit tesla (T). They are related as $\mathbf{B} = \mu_0\, \mathbf{H}$, where $\mu_0 = 4\pi \times 10^{-7}$ T/Am, is the permeability of free space [18]. At low applied fields, the magnetization grows linearly with the applied field until it reaches a saturation magnitude. As the field strength increases, the constant-magnitude saturated magnetization vector rotates toward the applied field.

Let us first consider the linear magnetization region for relatively low applied fields. As stated in [18], the magnetization is related to the internal field by the susceptibility of the material $\mathcal{X}$ as

$$\mathbf{M} = \mathcal{X} \cdot \mathbf{H}_\mathrm{i}. \tag{14.2}$$

The internal field $\mathbf{H}_\mathrm{i}$ can be described as linear superposition of the applied field $\mathbf{H}_\mathrm{d}$ and a demagnetizing field

$$\mathbf{H}_\mathrm{i} = \mathbf{H} + \mathbf{H}_\mathrm{d}. \tag{14.3}$$

The demagnetizing field $\mathbf{H}_\mathrm{d}$ is related to the magnetization by a tensor N of demagnetization factors based on the body geometry as $\mathbf{H}_\mathrm{d} = -N\mathbf{M}$. The matrix N is diagonal if the body coordinate frame is defined such that it aligns with the principle axes of the body: $N = \mathrm{diag}(n_x, n_y, n_z)$. Combining the earlier assumptions, we can relate the magnetization to the applied field by a susceptibility tensor

$$\mathbf{M} = \mathcal{X}_\mathrm{a} \cdot \mathbf{H}_\mathrm{i} \tag{14.4}$$

with a tensor of the form

$$\mathcal{X}_a = \mathrm{diag}\left(\frac{\mathcal{X}}{1 + n_x\mathcal{X}}, \frac{\mathcal{X}}{1 + n_y\mathcal{X}}, \frac{\mathcal{X}}{1 + n_z\mathcal{X}}\right). \tag{14.5}$$

$\mathbf{M}$, $\mathbf{H}$ and $\mathcal{X}_a$ are all written with respect to the body frame. Because of symmetry of the elliptical body, we need only to consider two demagnetization factors—the factor along the axis of symmetry n_a, and the factor in all radial directions

perpendicular to the axis of symmetry n_r. For relatively large susceptibility values, as they are typical for soft magnetic materials on the order of 10^3–10^6, and if we assume the demagnetization factors are not too close to zero, we can approximate (14.5) with

$$\mathcal{X}_a = \text{diag}\left(\frac{1}{n_a}, \frac{1}{n_r}, \frac{1}{n_r}\right). \tag{14.6}$$

From (14.5) we can see that magnetization is insensitive to changes in susceptibility if the susceptibility is relatively high. And in turn, the susceptibility is dominated by the body geometry, since it is determined by the demagnetization factor, which is a geometry-dependent value. The demagnetization factors for general ellipsoid bodies are part of the well-understood results of magnetostatics and were first computed in 1945 [25]. Generally, they are related by the constraint $n_x+n_y+n_z = 1$. We can rewrite this for an axially symmetric body as $n_a+2n_r = 1$. To understand the influence of the geometry on the magnetization vector, we need to look at the magnetization angle ϕ that describes the offset between the magnetization vector and the body symmetry axis. The longer the axis of the body, at constant radial dimension, the smaller the angle will become, since the demagnetization factor n_a along the body's symmetry axis will get smaller and, hence, the magnetization along this axis stronger. This can be understood from the following expressions:

$$n_a = \frac{1}{R^2-1}\left(\frac{R}{2\sqrt{R^2-1}}\ln\left(\frac{R\sqrt{R^2-1}}{R-\sqrt{R^2-1}}\right)-1\right) \quad \text{(prolate ellipsoid)} \tag{14.7}$$

$$n_a = \frac{R^2}{R^2-1}\left(1-\frac{R}{\sqrt{R^2-1}}\sin\left(\frac{R+\sqrt{R^2-1}}{R-\sqrt{R^2-1}}\right)\right) \quad \text{(oblate ellipsoid)}, \tag{14.8}$$

where $R \geq 1$ is the ratio of the long and short dimensions of the body. We can compute the magnetization angle ϕ directly, assuming (14.5), as

$$\phi = \tan^{-1}\left(\frac{n_a}{n_r}\tan\theta\right), \tag{14.9}$$

Thus, the larger R gets, the smaller n_a, and hence the smaller the angle ϕ. The offset angle between ϕ and θ determines how much the body is turning in order to align its magnetization axis with the vector of the applied field which is known as the torque. For a uniform magnetization throughout the body, we assume the volume contributes linearly to the torque and force that the body experiences in an applied external field. This assumption is fairly reasonable for small shapes with high aspect ratios. Hence, we can express the magnetic torque acting on the body in an applied external field as

$$T = \mu_0 v \mathbf{M} \times \mathbf{H}, \tag{14.10}$$

where v is the volume of magnetic material in m^3. The torque, in Newton meters, acts on the magnetic moment of the body such that $\mathbf{M}$ aligns with the direction of the magnetic field. A soft magnetic material in a magnetic field will become magnetized along its long axis, also called its easy axis and the torque tends to align the longest axis of the body with the field.

From (14.9) we can already see that for a soft magnetic sphere, where $n_x = n_y = n_z$ or $n_a/n_r = 1$ applies, there will be no torque acting on the body, since the magnetization vector and the field vector are always aligned which each other. This assumes the absence of any remanent magnetization. However, when taking hysteresis effects into account, the magnetization along the field vector will always be dominant and almost no rotational movement can be translated. This is why, if rotary motion of magnetic beads is required, a permanent magnetic material is generally used.

If the magnetization vector computed in (14.4) results for a certain applied field $\mathbf{H}$ in a smaller magnitude than the saturation magnetization m_s of the material, then we take $\mathbf{M}$ and ϕ as accurate. However, for $|\mathbf{M}| > m_s$, we move into the saturated-magnetization region. We set $|\mathbf{M}| = m_s$ and compute the rotation of $\mathbf{M}$ by minimizing the magnetic energy with respect to ϕ

$$e = \frac{1}{2}\mu_0 v(n_r - n_a)m_s^2 \sin^2\phi - \mu_0\, v m_s |\mathbf{H}| \cos(\theta - \phi), \tag{14.11}$$

where e is the energy in units of Joule. This equation is typically applied as a model for single magnetic-domain samples, but it is a good approximation of a multidomain body once saturation has been reached. To minimize e in (14.10), we get the derivative of e and equalize it to zero

$$(n_r - n_a)m_s \sin(2\phi) = 2|\mathbf{H}| \sin(\theta - \phi). \tag{14.12}$$

$\mathbf{M}$ will rotate such that ϕ satisfies (14.11). Within that model the magnetization vector $\mathbf{M}$ changes continuously with changes in the applied field $\mathbf{H}$, as proven in [18].

Due to the dominant magnetic shape anisotropy, it is in general more appropriate to use bodies with a preferred magnetization axis, the easy axis. For example, this applies for a cylindrical nanowire. We can apply the same constraints to any shape by equating them to ellipsoids. Improving these approximations has been the object of numerous studies, especially for cylinders [26, 27]. From [24] we can extract the demagnetization factor along a cylinder axis based on the model of an equivalent ellipsoid. For a cylinder of length l and radius r with aspect ratio $\tau = l/2r$ the following expression for the demagnetization factor along the cylinder's axis applies:

$$n_a^{\mathrm{cyl}}(\tau) = 1 + \frac{4}{3\pi\tau} - F\left(-\frac{1}{\tau^2}\right), \tag{14.13}$$

with $F(x) \equiv {}_2F_1\left[-\frac{1}{2},\ \frac{1}{2},\ 2,\ x\right]$, which is defined by the Gaussian hypergeometric function ${}_2F_1(a,\ b,\ c,\ z)$.

Let us consider ferromagnetically filled carbon nanotubes to be magnetized. We assume common design parameters such as a length $l = 1$ μm and a radius $r = 50$nm. Computing (14.13) with these values, where a piecewise polynomial approximation of ${}_2F_1$ is created, we get $n_a = 0.0412$, and therefore $n_r = 0.4794$, and the cylinder long axis is the easy axis. For precise and fast alignment performance, we try to maximize the magnetic torque T in (14.10) and look for the external field needed to fully magnetize the body for a maximum $\mathbf{M}$. For a soft magnetic body this means reaching the saturation magnetization m_s. The resulting magnetization dependent on the externally applied magnetic field is given by combining (14.3) and (14.4) as

$$\mathbf{M} = \frac{\mathcal{X}}{1 + \mathcal{X}N}\mathbf{H}, \tag{14.14}$$

which can be approximated as $\mathbf{M} = \frac{1}{N}\mathbf{H}$ for high $\mathcal{X}$, as for nickel ($\mathcal{X} = \mu_r - 1 = 599$).

If we apply a field parallel to the body's long axis, which we set to be coplanar with the x-axis of the coordinate frame, and we set $\mathbf{M} \equiv m_\mathrm{s}$ for the desired reach of the saturation magnetization, we get $|\mathbf{H}_\mathrm{sat}| = n_a \cdot m_\mathrm{s}$ for the field required to fully magnetize the body. This, however, involves the assumption that the body is fully, uniformly magnetized along its long axis.

With the magnetic moment, we can now apply a torque and orient the object as desired. In addition, we can apply a force on the magnetized body and pull the object along its long axis, which is the topic of the next subchapter.

14.2.3 Pulling Through Fluids by Applied Magnetic Gradients

When a magnetic body is subjected to an externally applied magnetic field, it will experience a torque aligning its long axis with the direction of the applied field. Let us set the field vector coplanar with the x-axis of the coordinate frame. Now, if we apply a magnetic gradient that is coplanar with the x-axis, the object will experience a force and is pulled along its long axis. More generally, the magnetic force that body experiences can be expressed as

$$\mathbf{F} = \mu_0 v(\mathbf{M} \cdot \nabla)\mathbf{H}. \tag{14.15}$$

When pulling a magnetic object through Newtonian fluid at low Re, the object nearly instantaneously reaches its terminal velocity ϑ where the viscous drag force, which is linearly related to velocity through a drag coefficient, exactly balances the applied magnetic force $\mathbf{F}$.

We can approximate the magnitude of the required magnetic field gradient needed to accelerate the body until drag force and magnetic force are in equilibrium and a certain body velocity, such as one body length per second, is reached. Since no electric current is flowing through the region occupied by the body, Maxwell equations provide the constraint $\nabla \times \mathbf{B} = 0$. This allows us to express (14.15) in the more intuitive form

$$\mathbf{F} = v(\nabla \cdot \mathbf{B})^{\mathrm{T}}\mathbf{M}. \tag{14.16}$$

If we consider that the field gradient is a vector coplanar with the x-axis of the coordinate frame and the body is uniformly and fully magnetized along its long axis, which is coplanar with the x-axis, we get

$$\begin{pmatrix} F_x \\ F_y \\ F_z \end{pmatrix} = v \begin{pmatrix} \frac{\partial B_x}{\partial x} & 0 & 0 \\ 0 & 0 & 0 \\ 0 & 0 & 0 \end{pmatrix}^{\mathrm{T}} \cdot \begin{pmatrix} m_{\mathrm{s}} \\ 0 \\ 0 \end{pmatrix}. \tag{14.17}$$

We assume only an axial contribution of the field gradient in x-direction and no field and field gradient applied along the y- and z-axis. From classical hydrodynamics we know that drag force can be expressed as

$$\mathbf{F}_{\mathrm{drag}} = D \cdot \vartheta, \tag{14.18}$$

where ϑ is the velocity of the object and D is the fluid and object dependent drag coefficient. For a spherical bead of diameter d, the translational drag coefficient is described as Stokes flow as [28]

$$D_{\mathrm{sphere}} = 3\pi\eta d. \tag{14.19}$$

For slender bodies, such as very thin cylindrical objects, resistive force coefficients (RFC) can be used [29], and the drag coefficient can be approximated as

$$D_{\mathrm{cylinder}} = \frac{2\pi\eta l}{\ln\left(\frac{l}{r}\right) - 0.807}. \tag{14.20}$$

The required gradient $\partial B_x/\partial x$ can be determined when the magnetic force $\overrightarrow{F}$ is identified with the drag force $\mathbf{F}_{\mathrm{drag}}$ and by defining a desired velocity vector along the x-axis.

14.3 Generating Magnetic Fields and Gradients

14.3.1 State of the Art

Controlled magnetic fields can be generated by stationary current-controlled electromagnets [17], as shown in Fig. 14.3, by electromagnets that are position and current controlled [30], by position-controlled permanent magnets, or even by a commercial magnetic resonance imaging (MRI) systems [31]. In any case, the rapid decay of magnetic field strength with distance from its source creates a major challenge for magnetic control.

Permanent magnets generate strong fields on a per volume basis, however, obstacles such as the interaction between adjacent magnets and the requirement of a certain shielding mechanism in order to "turn off" the magnetic field must be considered. In order to control the field strength the magnets need to be externally actuated. In comparison, air-core solenoids have rather weak fields compared to permanent magnets, but field contributions superpose linearly, so current controls the field strength and the field can be switched off instantly.

A common approach to the generation of homogenous fields is the use of Helmholtz coil configurations. By positioning three pairs orthogonal to each other a 3-degree-of-freedom system is achieved. The magnetic propulsion methods discussed above use Helmholtz coils, Maxwell coils, or various combinations thereof, that entirely surround the workspace to generate the desired field strength and orientation. Figure 14.3 shows a typical Helmholtz configuration.

In such a 3 DOF system, the direction of the magnetic field and the magnetic gradient are dependent on each other, meaning that a nonspherical object cannot be freely navigated. This system is consequently nonholonomic, i.e., there exist constraints that prevent the object from moving instantaneously in some directions.

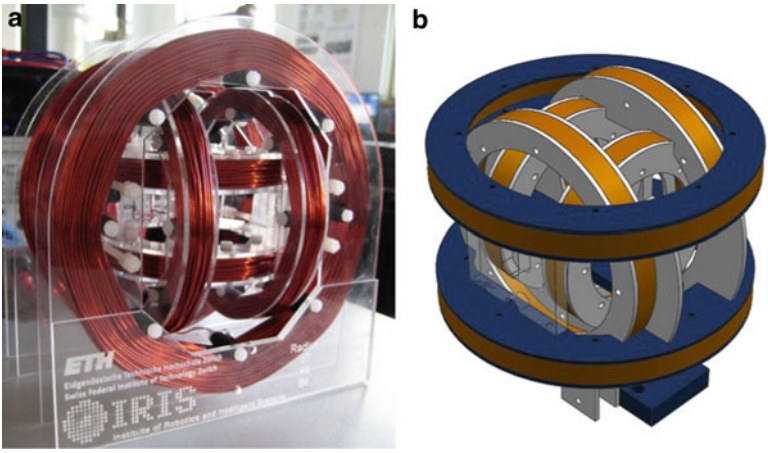

Fig. 14.3 Example of a Helmholtz coil configuration. (**a**) real configuration, (**b**) model

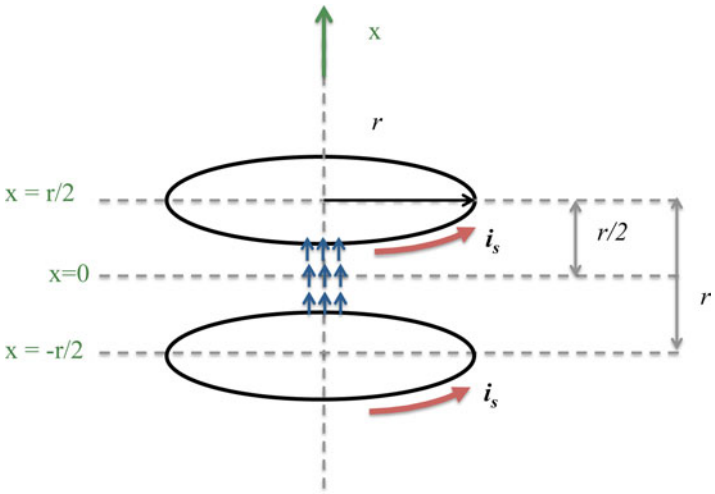

Fig. 14.4 Electromagnetic coils in Helmholtz configuration as field-generation hardware for microrobot propulsion. Uniform magnetic fields in the center of the workspace are generated by current flowing in the same direction

14.3.1.1 Calculating Magnetic Fields and Gradients Generated by Solenoids

Consider a single current loop l at a distance $r/2$ from the origin of the axis. We can express the magnetic field B_x^l along its axis (off-axis field is not considered) generated by a current i_s flowing through the conductor. From the Biot–Savart rule we get

$$B_x^l(x,i_s) = \mu_0 \frac{i_s r^2}{2\left(r^2 + \left(\frac{r}{2} - x\right)^2\right)^{3/2}}, \tag{14.21}$$

where x is the distance along the axis of the coil from its center, and r is the radius of the current loop. For generating higher fields, we can extend the current loop to a solenoid s consisting of n wire turns. A total current $I = n \cdot i_s$ flows then through the coil and the generated field can be expressed as

$$B_x^s(x,i_s) = \mu_0 n \frac{i_s r^2}{2\left(r^2 + \left(\frac{r}{2} - x\right)^2\right)^{3/2}}. \tag{14.22}$$

Now, if we would like to generate a homogenous field over a larger volume of space, we add another solenoid at a distance r from the first solenoid plane, at the position $x = -r/2$, as shown in Fig. 14.4.

We can linearly superpose the two fields generated by the same current i_s flowing through both coils as

$$\begin{aligned} B_x(x,i_s) &= B_x^1(x,i_s) + B_x^2(x,i_s) \\ &= \frac{\mu_0 n}{2}\left(\frac{i_s r^2}{\left(r^2+\left(\frac{r}{2}-x\right)^2\right)^{3/2}} + \frac{i_s r^2}{\left(r^2+\left(\frac{r}{2}+x\right)^2\right)^{3/2}}\right). \end{aligned} \tag{14.23}$$

At the center point of the two coils we get now the axial component of the field in x-direction as

$$B_x(0,i_s) = \left(\frac{4}{5}\right)^{3/2}\frac{\mu_0 n i_s}{r}. \tag{14.24}$$

Note that this is an accurate expression for on-axis field computation and does not cover the off-axis field. The off-axis field calculation is nontrivial and in most cases there is no closed-form analytic solution. It is reasonable, though, to assume a homogenous field for a certain small workspace around the center point at $x = 0$. For Helmholtz coils this can usually be stated for a volume around the center point as large as 5 % of the distance between the coil planes. Another assumption is that the thickness of the wire is considered infinitesimally small and, hence, the coil is considered a plane with no expansion along the x-axis. For long solenoids with many wire turns or with thick wire, the expression in (14.23) must be integrated over the length a of the coil from $x = r/2$ to $x = r/2 + a$.

In order to obtain 3-DOF control, we add two more pairs of coils in an orthogonal arrangement as previously mentioned and shown in Fig. 14.3. We can now build up the field vector $\mathbf{B}(\mathbf{P}) = \left[B_x(\mathbf{P}), B_y(\mathbf{P}), B_z(\mathbf{P})\right]$ at a point $\mathbf{P} = [x, y, z]^{\mathrm{T}}$ of the workspace consisting of the three axial contributions of each coil pair.

To generate a gradient an additional coil pair for each axis can be added. The current in the gradient pair is of same magnitude, but in the opposite direction (Fig. 14.5).

The magnitude of the field gradient at a certain point along the axis can be obtained by the derivative of $B_x'(x,i_s) = B_x^1(x,i_s) - B_x^2(x,i_s)$, where the contributions of the two coils are subtracted according to the inverse current flow. The system consists of 12 solenoids but only 6 current inputs.

An alternative is to work with a single coil pair in each direction for both the generation of field and gradient, resulting in a system of 6 solenoids but controlling each current independently. In other words, a gradient can also be generated with a classic Helmholtz configuration by applying a higher current in one coil of the pair than in the other, with the result of a constant gradient and homogenous field in the center of the two coils.

Depending on the design constraints other variations, such as Maxwell coils, can be employed through a similar derivation.

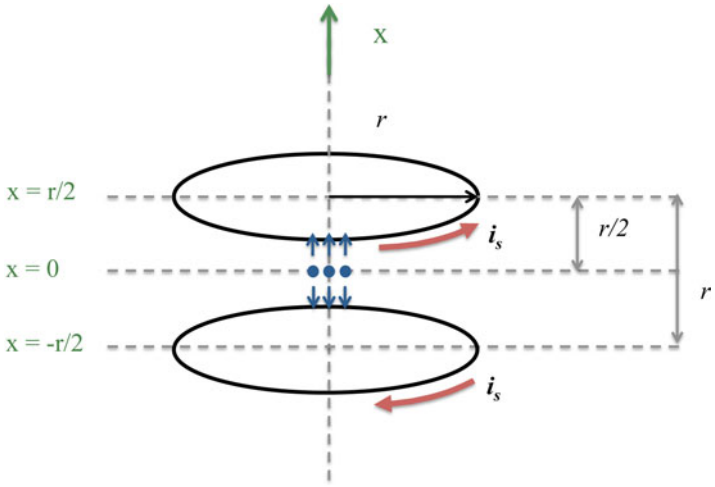

Fig. 14.5 Maxwell coil configuration. Gradient fields can be generated by running the current in opposite directions

14.3.1.2 General Control System

Within a given set of air-core electromagnets, each electromagnet creates a magnetic field throughout the workspace that can be computed for any point **P** of the workspace and any given electromagnet e. We express this field as a vector $\mathbf{B}_e(\mathbf{P})$ From (14.21), the field created by of a solenoid, we know that the field depends linearly on the current i_s through the air-core electromagnet. Hence, we can express $\mathbf{B}_e(\mathbf{P})$ for each electromagnet as a unit-current vector in units T/A multiplied by a current value i_e in units A [32, 33] as

$$\mathbf{B}_e(\mathbf{P}) = \widetilde{\overrightarrow{B}}_e(\mathbf{P}) i_e. \tag{14.25}$$

Since the field contributions of the individual currents superimpose linearly, this can be denoted by the $3 \times n$ unit-field contribution matrix $\mathcal{B}(\mathbf{P})$

$$\mathbf{B}(\mathbf{P}) = \left[\tilde{\mathbf{B}}_1(\mathbf{P}) \ldots \tilde{\mathbf{B}}_n(\mathbf{P})\right] \begin{bmatrix} i_1 \\ \vdots \\ i_n \end{bmatrix} = \mathcal{B}(\mathbf{P})\mathbf{I}. \tag{14.26}$$

This also applies for electromagnets with soft magnetic cores, if the material used resembles an ideal soft magnetic material with negligible hysteresis and the cores are kept within their linear regions.

Furthermore, we can express the gradient of the field in a given direction in a specific frame, e.g., the x direction, as the contributions from each of the currents

$$\frac{\partial \mathbf{B}(\mathbf{P})}{\partial x} = \begin{bmatrix} \frac{\partial \tilde{\mathbf{B}}_1(\mathbf{P})}{\partial x} \cdots \frac{\partial \tilde{\mathbf{B}}_n(\mathbf{P})}{\partial x} \end{bmatrix} \begin{bmatrix} i_1 \\ \vdots \\ i_n \end{bmatrix} = \mathcal{B}_x(\mathbf{P})\mathbf{I}. \tag{14.27}$$

To control a nonspherical magnetic body, we need to precompute the magnitude of the magnetic field (to apply a desired torque to orient the body) and the magnetic gradient **G** (to apply a desired force to move the body) at a certain point **P**. This can be combined as

$$\begin{bmatrix} \mathbf{B} \\ \mathbf{G} \end{bmatrix} = \begin{bmatrix} B(\mathbf{P}) \\ \hat{\mathbf{B}}^{\mathrm{T}} B_x(\mathbf{P}) \\ \hat{\mathbf{B}}^{\mathrm{T}} B_y(\mathbf{P}) \\ \hat{\mathbf{B}}^{\mathrm{T}} B_z(\mathbf{P}) \end{bmatrix} \begin{bmatrix} i_1 \\ \vdots \\ i_n \end{bmatrix} = \mathcal{A}(\hat{\mathbf{B}}, \mathbf{P})\mathbf{I}. \tag{14.28}$$

The n electromagnet currents are mapped to a field and gradient through an $6 \times n$ actuation matrix $\mathcal{A}(\hat{\mathbf{B}}, \mathbf{P})$ which depends on the orientation of the magnetic field and the set point. For a desired field/gradient vector, the currents required can be found using the pseudoinverse

$$\mathbf{I} = \mathcal{A}(\hat{\mathbf{B}}, \mathbf{P})\dagger \begin{bmatrix} \mathbf{B} \\ \mathbf{G} \end{bmatrix}. \tag{14.29}$$

If there are multiple solutions to achieve the desired field and gradient, the pseudoinverse finds the solution that minimizes the two-norm of the current vector, which is desirable for the minimization of both power consumption and heat generation. The pseudoinverse of $\mathcal{A}$ is of rank 5 corresponding to the no-torque generation about the magnetization axis, which is never possible. More details on this can be found in [32]. In order now to use (14.29), a unit-current field map must be constructed for each of the electromagnets. This can be done by analytical models, finite-element-method (FEM) data or system measurements.

14.3.2 A Hemispherical Electromagnetic System for 5-DOF Wireless Micromanipulation

The use of a Helmholtz coil configuration does not allow the generation of fields and gradients independently of one another; we are thus limited to nonholonomic manipulation performance for any full state control in 3D. To create a holonomic system with 5-DOF (3-DOF positioning and 2-DOF pointing orientation) wireless

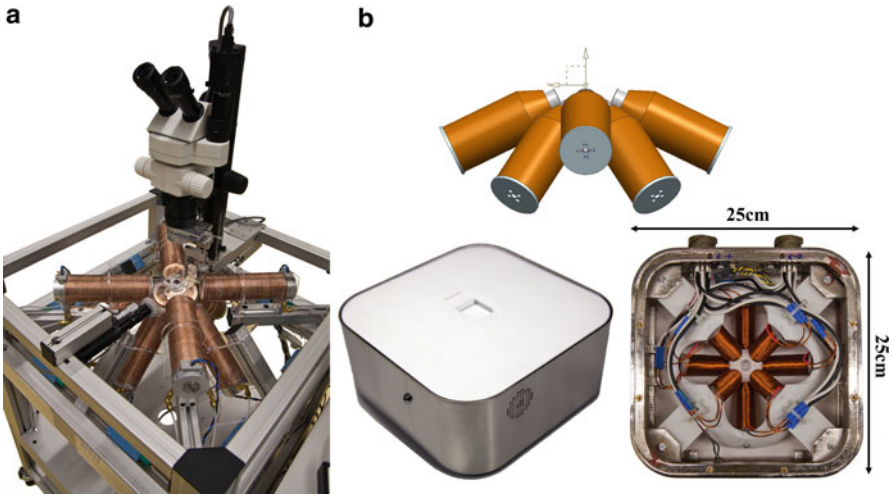

Fig. 14.6 (**a**) OctoMag system constructed at ETH Zurich [31] (**b**) *top* and *bottom right*: electromagnetic core arrangement as model and from *bottom view*; *bottom left*: *top view* of the system, a 30 mm × 30 mm area is available for sample placement [32]

control of a magnetic microrobot a different electromagnet configuration is needed. Stationary electromagnets are selected instead of permanent magnets that must be mechanically actuated. Air-core electromagnets are advantageous due to the linear superposition of the generated fields, but the fields are very weak unless superconducting coils are used. However, superconductors have slow slew rates. Alternatively, soft magnetic cores can be used to enlarge the field by a factor μ_r, which depends on the magnetic permeability of the core material. However, analytical modeling becomes more complicated, since the fields do not superimpose linearly. Though, if kept in their linear regions, this presents only a minor constraint on modeling and still offers a relatively large region of control.

So far, we have considered microrobotic control that relies on systems that fully surround the workspace. A technical difficulty lies in scaling the system to create an interior volume that is relatively large. Based on the control system explained in Sect. 14.3.1 and by leaving the number of electromagnets open, an optimization problem can be created that results in a new system with a unique coil configuration. The system enables the control of a microrobot through a large workspace while being completely unrestrained in rotational DOFs. The system is called the OctoMag (see Fig. 14.6a) and is discussed in detail in [32].

In a modification of the OctoMag, the location of the electromagnets is restricted to a single hemisphere. This allows more physical freedom in the workspace and allows the system to be compatible with an inverted microscope. This system, called the MiniMag, is shown in Fig. 14.6b [33]. With its much smaller size it also fits under conventional tabletop microscopes and is easily transportable.

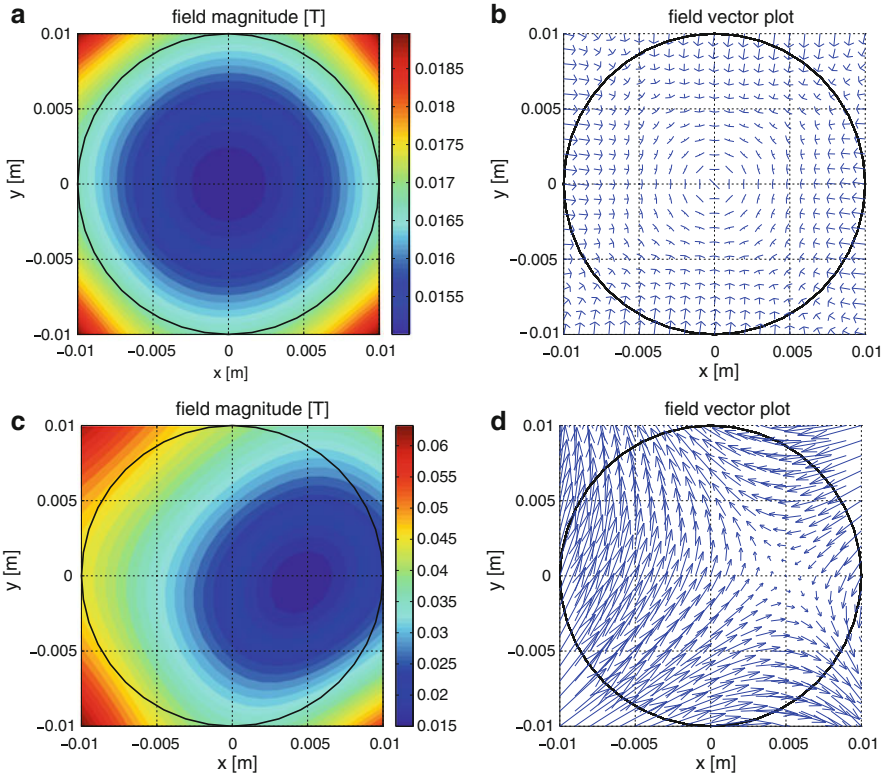

Fig. 14.7 Theoretical field magnitude (**a**, **c**) and orientation (**b**, **d**) at $z = 0$ of the workspace when the system is commanded to a 15 mT field along the positive z-axis at [0.000, 0.000, 0.000] (**a**, **b**) and at [0.005, 0.000, 0.000] (**c**, **d**). The figure illustrates a more homogeneous region when the set point is at the center of the workspace than toward the extremities, which reduces the need for position feedback when working within a small workspace (reprinted with permission from [32])

14.3.2.1 System Design

An optimal magnetic manipulation system can be designed using n electromagnets [32]. Given a design criteria of an isotropic task space, a configuration with eight electromagnets, arranged as illustrated in Fig. 14.6, results in the best performance. Intuition might lead one to believe that electromagnets must uniformly surround the workspace in order to create the desired isotropic behavior, but this is not the case. With the configuration shown in Fig. 14.6, pushing, pulling, and lateral forces can be exerted while maintaining any desired microrobot orientation.

Using (14.29) for control requires knowledge of the microrobot's pose. Figure 14.7 depicts the contour plots of a magnetic field of 15 mT along positive z, set for the position **P** at the origin of the magnetic workspace (a, b) and for a position 5 mm off center (c, d). The generated field is inhomogeneous and increases towards

the extremities. The set point of the magnetic field defines an unstable equilibrium position from where the field magnitude increases equally in all directions. The instability of this equilibrium causes magnetic agents to drift, as dictated in theory by Earnshaw's theorem. For drift minimization, the magnetic agent needs to be kept in the unstable equilibrium state by setting the magnetic field at its updated location.

For open-loop control experiments, the set point can be left at the origin of the system if we limit the physical workspace. Then, we can assume that the magnetic field does not significantly vary across that area (Fig. 14.7a, b) and the drift is minimal. Hence, we can eliminate the need for any localization of the micro/nanorobot. This assumption is reasonable in the case of objects ranging on the order of nanometers or tens of micrometers that use workspaces smaller than $500\ \mu m^3 \times 500\ \mu m^3 \times 500\ \mu m^3$. For applications that require a larger workspace, the set point needs to be updated through vision-based agent localization (Fig. 14.7c, d). However, as the set point approaches the boundaries of the workspace, higher inhomogeneities are appearing.

Closed-loop servoing requires an additional control loop, wherein the error between the desired and the current position of the object is used as input to a PID controller that calculates the desired magnetic field strength and gradient. With closed-loop position control the drift is compensated for.

There are a number of methods to generate the current field maps that are required for the control system. One can either explicitly measure the magnetic field of the final, constructed system at a grid of points, or one can compute the field values at a grid of points using FEM models. For every single electromagnet a unit-current field map must be calculated as shown in (14.25). In the event that a given electromagnet configuration exhibits geometrical symmetry, it is possible to calculate fewer maps and then rotate them during run time using homogeneous transformations. The point dipole model is chosen as analytical model for fast computational reasons. This approximation is suitable for solenoids and cylindrical magnets, also derived in [34].

14.3.2.2 System Performance

MiniMag is capable of producing magnetic fields in excess of 20 mT and field gradients of 2 T/m up to 2 kHz and with OctoMag fields up to 50 mT and gradients of 2 T/m up to 10 Hz can be reached. The frequency response is in latter case slower, since the coils have higher inductance and higher voltages need to be applied to drive the system. Although MiniMag was originally designed for gradient control of microobjects, a variety of different control methods are possible, e.g., stepping or rotational modes. Figure 14.8 demonstrates a microrobot moving on a circle trajectory while levitating in a plane under closed-loop servo control. The servo control was performed with a simple proportional controller to the target point. The tilt visible in the trace is due to the fact that the drift in the system varies slightly across the workspace due to calibration and modeling inaccuracies, which are not taken into consideration in the controller causing it to be biased.

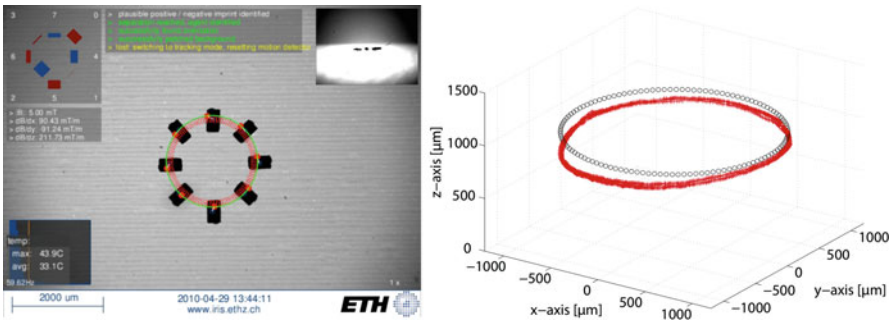

Fig. 14.8 Time-lapse image of a permanent magnetic agent being servoed along a circular trajectory in the MiniMag. The image shows a *top view* of the experiment, while the picture-in-picture inset shows a *side view*. The trace on the *right image* shows tracked data for the duration of the experiment. The *circles* indicate the target way points while the *pluses* show the tracked position. The average trajectory completion time is 7.14 s (reprinted with permission from [32])

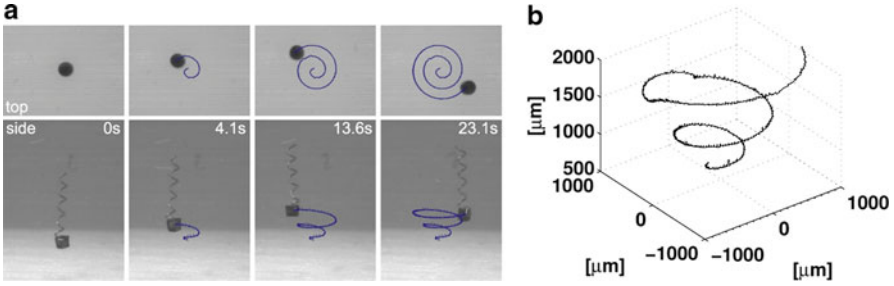

Fig. 14.9 Hybrid swimming/gradient strategy. The agent is rotated at a speed sufficient for gravity compensation and the small gradients on the order of 50–100 mT/m are used to servo the agent through the trajectory [32]

As an alternate propulsion method, swimming strategies can be implemented for microrobotic control through the use of rotating magnetic fields [11]. Figure 14.9 shows results of using the MiniMag for this type of control. In this experiment we first levitate a helical swimmer with a 380 µm large SmCo head and an approximately 2,000 µm long Cu tail into the center of the workspace using gradient control. A rotational magnetic field around the z-axis at different frequencies with no gradient is applied and the corresponding average vertical velocities are recorded. When the rotation frequency is small, the swimmer does not exert as much force as gravity and falls. At 25–50 Hz the agent generates enough force to lift itself, and at frequencies beyond this it moves in the vertical direction.

The system is capable of 5-DOF control while occupying a single hemisphere and providing an open workspace. It provides precise positioning under closed-loop control with computer vision but can also be used with no visual tracking, relying only on visual feedback from the human operator during teleoperation.

14.4 Fabrication of Magnetic Drug Carriers

14.4.1 Overview

In the past 20 years, several synthetic methods for the fabrication of nanostructures such as nanoparticles, nanohelices, nanotubes, and nanowires (NWs) have been proposed. Miniaturization of devices towards the nanoscale is important for many new applications in biotechnology and medicine. In the field of micro- and nanorobotics, these nanostructures provide a potential biomedical platform for controlled, noninvasive medicine. The treatment of cancer is one of the most pursued directions in these fields. Procedures like chemotherapy, radiation therapy, and surgery are applied and succeed in several cases; however, they are far from being efficient. A major drawback is the inability to specifically target cancer cells; hence, healthy regions become traumatized. As an alternative, the use of multifunctional magnetic nanomaterials that specifically target cancer cells has been proposed [35]. These materials can be used for better imaging of tumors, and to locally deliver anticancer drugs simultaneously. Among the variety of magnetic nanostructures available, NWs or nanotubes are advantageous over others due to their high aspect ratio and magnetic shape anisotropy. Carbon nanotubes (CNTs) are probably the most widely studied nanostructure, due to their extraordinary mechanical and physicochemical properties. A wide variety of applications, including biomedical devices for diagnostics and drug delivery, have been proposed. Since carbon nanotubes can be functionalized both endohedrally and exohedrally, they can be used as multifunctional nanocarriers for targeted drug delivery [35].

14.4.2 Magnetic Nanoparticles

Magnetic nanoparticles (MNPs) represent one major class of nanoscale materials and a tremendous amount of work has been carried out to better address clinical needs through specific design, synthesis, and surface functionalization of MNPs. Potential applications can be divided into two major areas, MNPs for MR imaging and for drug delivery. In MRI technology, they can be used for cancer imaging, cardiovascular disease imaging, and molecular imaging. Next-generation MNP-based MRI contrast agents and carriers for drug delivery incorporate novel nanocrystalline cores, coating materials, and functional ligands to improve the detection and specific delivery of these nanoparticles [36].

MNPs can be generally classified into two main groups: ceramics, such as iron oxide and barium ferrite, metallic NPs and alloys, such as cobalt, nickel, iron, and combinations thereof containing at least one ferromagnetic element. Numerous synthetic methods have been developed to synthesize MNPs such as coprecipitation, sol–gel synthesis, microemulsion synthesis, sonochemical reaction, hydrothermal reaction, thermal decomposition, electrospray synthesis, and laser pyrolysis [37].

Methods to fabricate iron oxide NPs vary from classical wet chemistry solution based methods to laser pyrolysis or chemical vapor deposition (CVD) [38]. Iron oxide NPs are particularly attractive due to their biocompatibility and ease of fabrication. Metallic NPs, such as those made of iron or nickel, tend to be chemically unstable. However, since iron nanoparticles are attractive due to their high saturation magnetization, ways to improve stability have been pursued. As a result, core-shell techniques such as the coating with magnetite (Fe_3O_4), gold, or biocompatible silica have been suggested. Concerning metal-alloy NPs, combinations of metals can be synthesized that exhibit superparamagnetic properties or that possess high magnetocrystalline anisotropy such as FePt [37].

There are numerous strategies to functionalize MNPs depending on the type of MNP and purpose of the functionalization. For biocompatibility reasons an additional coating is often required. For the purpose of drug delivery, suitable drug molecules have to be attached, preferably in a manner so that they can also be released. For optical imaging probes, fluorescent dyes are added. With advancements in DNA technology, the delivery of genes attached to MNPs may present a potential application.

14.4.3 Fabrication of Magnetic Nanowires

Most magnetic nanowires for applications in biomedicine are fabricated by the use of nanoporous templates and a subsequent electrodeposition of the required metal [39]. This method of template synthesis has become popular for the preparation of cylindrical materials in a facile, high-throughput and cost-effective way [40]. As described above for nanoparticles, surface functionalization is also pursued for NWs. Among this wide range of nanomaterials, carbon nanotubes are particularly interesting. Their unique electrical, mechanical, and optical properties are already widely exploited; however, they are also superb candidates for various functionalization methods. They offer strong covalent bonds as well as weaker π-π-stacking and hydrophobic wrapping. CNTs combined with magnetic nanowires create a device amenable to magnetic manipulation. Filling CNTs with a ferromagnetic material results in an object that becomes most easily magnetized along its long axis.

Several approaches have been adopted to fill the core of carbon nanotubes with ferromagnetic materials like Ni, Co, and Fe including

1. Pyrolysis, where formation and filling of carbon nanotubes occur simultaneously [41–43].
2. Step-by-step approach, where during the growth process of the CNT their caps are removed and magnetic material diffuses inside the tubule [44, 45].
3. Template-assisted growth of carbon nanotubes followed by electrodeposition of metal catalysts inside the pores of a template [46, 47].

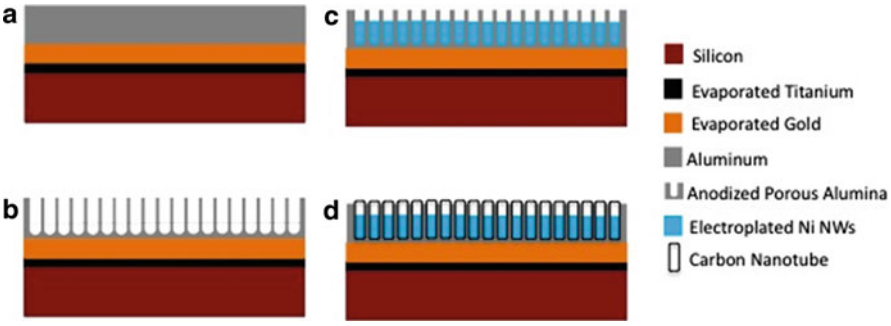

Fig. 14.10 Fabrication steps of the Ni-filled CNTs: (**a**) Silicon wafer with evaporated Al on *top*; (**b**) Anodization process; (**c**) Electrodeposition of Ni NWs (**d**) CNT growth

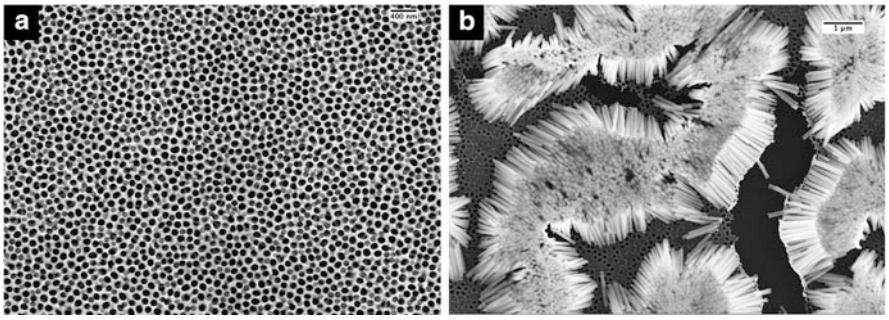

Fig. 14.11 (**a**) SEM image of AAO template. The pore diameter distribution is 110 ± 10nm (**b**) Array of Ni NWs after selective etching of the AAO template

The template-assisted synthesis has become a widely adopted fabrication technique. The process steps to fabricate ferromagnetic nickel nanowire cores encapsulated in a carbon nanotube shell by the use of template-assisted electrodeposition and growth is shown in Fig. 14.10.

The sequence starts with the fabrication of a suitable template for NW synthesis [35]. Aluminum is evaporated on a layer of gold and titanium on a silicon surface and a subsequent anodization process transforms the layer into porous alumina (AAO) (Fig. 14.11a). Anodization of aluminum is tunable with regards to both diameter and length depending on the operating conditions such as anodizing voltage and time. AAO templates also produce arrays of carbon nanotubes of equal dimensions thereby making it possible to have a standardized growth process for large-scale production. An array of uniform pores of e.g., 100nm diameter and 1 μm depth (which is defined by the thickness of the aluminum layer) can be achieved.

Next, nickel is deposited inside the pores by galvanostatic pulse current (PC) electrodeposition. Eletrodeposition is an effective method for growing 1D nanostructures in a controlled way without the implementation of expensive instrumentation, high temperatures or low-vacuum pressures. A result of a batch of Ni NWs after template release is illustrated in Fig. 14.11b.

Fig. 14.12 Hybrid CNT-based magnetic nanostructures arranged on the silicon surface after release of the template

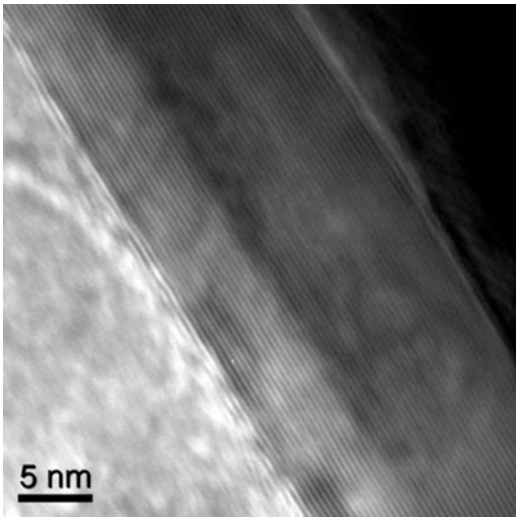

Fig. 14.13 High resolution TEM image demonstrating graphitic shells encapsulating a Ni NW. the thickness of the shells is 17.65nm whereas the interlayer distance is 0.345nm which corresponds to 50 shells

After PC electrodeposition, low-pressure chemical vapor deposition (LPCVD) is utilized to coat nanowires with graphitic as shown in Figs. 14.12 and 14.13.

Finally, the AAO template is dissolved, e.g., by NaOH, and the Ni-filled CNTs can be washed and dispersed in liquid. They are ready then for further exohedral functionalization such as the chemical attachment of fluorescent dyes for tracking and drug molecules for targeted delivery. Considering the manipulation,

the graphitic volume was neglected in the above estimations, which increase the drag force and decrease the actual magnetic volume per drug carrier. However, the thickness of the shell layer varies widely and was not considered due to simplicity.

As mentioned earlier, there are numerous techniques to fabricate cylindrical hybrid magnetic drug carriers. However, the template-assisted technique was described here more in detail, since it is a facile batch-fabrication method that allows a uniform coating of ferromagnetic nanowires with high quality graphene layers for biomedical functionalization.

14.5 Conclusion

This chapter focuses on methods of generating multi degree-of-freedom magnetic fields and gradients to wirelessly control nanorobots with potential applications in targeted drug delivery. Recent developments in fabricating magnetic nanodevices that can be used for biomedical applications indicate this area of research has great potential. The field of nanorobotics requires the expertise of several disciplines including medicine, biology, physics, micro-/nanosystem technology, hardware engineering, and computer science and is pushing research in fabrication of optimal nanostructures for the use as minimally invasive platforms.

References

1. Lymberis A (2010) Micro-nano-biosystems: an overview of European research. Minim Invasive Ther 19:136–143
2. Nelson BJ (2010) Microrobots for minimally invasive medicine. Annu Rev Biomed Eng 12: 55–85
3. DiSalvo FJ (1999) Thermoelectric cooling and power generation. Science 285(5428):703–706
4. Kasap SO (2006) Principles of electronic materials and devices, 3rd edn. McGraw-Hill, New York, NY
5. Popovic M et al (2006) Electromagnetic induction. In: Bansal R (ed) Fundamentals of engineering electromagnetics. Taylor & Francis, Boca Raton, FL
6. Theodoridis MP, Mollov SV (2005) Distant energy transfer for artificial human implants. IEEE Trans Biomed Eng 52(11):1931–1938
7. Lenaerts B, Puers R (2007) An inductive power link for a wireless endoscope. Biosens Bioelectron 22(7):1390–1395
8. Guanying M et al (2007) Power transmission for gastrointestinal microsystems using inductive coupling. Physiol Meas 28(3):N9–N18
9. Furlani EP (2001) Permanent magnet and electromechanical devices: materials, analysis, and applications. Academic, San Diego, CA, p 518
10. Martel S et al (2007) Automatic navigation of an untethered device in the artery of a living animal using a conventional clinical magnetic resonance imaging system. Appl Phys Lett 90(11):114105-1–114105-3
11. Abbott JJ et al (2009) How should microrobots swim? Int J Robot Res 28:1434–1447
12. Brennen C, Winet H (1977) Fluid mechanics of propulsion by cilia and flagella. Annu Rev Fluid Mech 9:339–398

13. Vogel S (2003) Comparative biomechanics: life's physical world. Princeton University Press, Princeton, NJ
14. Behkem B, Sitti M (2006) Design methodology for biomimetic propulsion of miniature swimming robots. ASME J Dyn Syst Meas Control 128:36–43
15. Kósa G, Shoham M, Zaaroor M (2007) Propulsion method for swimming microrobots. IEEE T Robotic Autom 23(1):137–150
16. Honda T, Arai KI, Ishiyama K (1996) Micro swimming mechanisms propelled by external magnetic fields. IEEE T Magn 32(5):5085–5087
17. Zhang L, Abbott JJ, Dong LX, Kratochvil BE, Bell D, Nelson BJ (2009) Artificial bacterial flagella: fabrication and magnetic control. Appl Phys Lett 94:064107
18. Abbott JJ (2007) Modeling magnetique torque and force for controlled manipulation of soft-magnetic bodies. IEEE T Robotic 23(6)
19. Jiles D (1991) Introduction to magnetism and magnetic materials. Chapman and Hall, London
20. O'Handley RC (2000) Modern magnetic materials: principles and applications. Wiley, New York, NY
21. Ergeneman O, Dogangail G, Kummer MP, Abbott JJ, Nazeeruddin MK, Nelson BJ (2008) A magnetically controlled wireless optical oxygen sensor for intraocular measurements. Sens J 8:29–37
22. Amblard F, Yurke B, Pargellis A, Leibler S (1996) A magnetic manipulator for studying local rheology and micromechanical properties of biological systems. Rev Sci Instrum 67(3): 818–827
23. Judy JW (1996) Batch-fabricated ferromagnetic microactuators with silicon flextures. Dissertation, University of California, Berkeley
24. Beleggia M, De Graef M, Millev YT (2006) The equivalent ellipsoid of a magnetized body. J Phys D Appl Phys 39:891–899
25. Osborn JA (1945) Demagnetizing factors of the general ellipsoid. Phys Rev 67(11/12):351–357
26. Joseph RI (1966) Ballistic demagnetizing factor in uniformly magnetized cylinders. J Appl Phys 37:4639
27. Chen DX, Brug JA, Goldfarb RB (1991) Demagnetizing factors for cylinders. IEEE Trans Mag 27(3601)
28. White FM (1991) Viscous fluid flow, 2nd edn. McGraw-Hill, New York, NY
29. Cox RG (1970) The motion of long slender bodies in a viscous fluid part 1. General theory. J Fluid Dyn 44:791–810
30. Yesin KB, Vollmers K, Nelson BJ (2006) Modeling and control of untethered bio-microrobots in a fluidic environment using electromagnetic fields. Int J Robot Res 25(5–6):527–536
31. Mathieu JB, Beaudoin G, Martel S (2006) Method of propulsion of a ferromagnetic core in the cardiovascular system through magnetic gradients generated by an MRI system. IEEE BioMed Eng 53(2):292–299
32. Kummer MP et al (2010) OctoMag: an electromagnetic system for 5-DOF wireless micromanipulation. IEEE T Robotic 26:6
33. Kratochvil BE et al (2010) MiniMag: a hemispherical electromagnetic system for 5-DOF wireless micromanipulation. In: Proceedings of IEEE ISER, New Delhi, India
34. Derby N, Olbert S (2010) Cylindrical magnets and ideal solenoids. Am J Phys 78(3a):229
35. Zeeshan MA et al (2011) Structural and magnetic characterization of batch-fabricated nickel encapsulated multi-walled carbon nanotubes. Nanotechnology 22:275713
36. Sun C, Lee JSH, Zhang M (2008) Magnetic nanoparticles in MR imaging and drug delivery. Adv Drug Deliv Rev., 60(11):1252–65
37. Hao R et al (2010) Synthesis, functionalization, and biomedical applications of multifunctional magnetic nanoparticles. Adv Mater 22:2729–2742
38. Tartaj P et al (2003) The preparation of magnetic nanoparticles for applications in biomedicine. J Phys D Appl Phys 36:182–197
39. Varadan VK, Chen L, Xie J (2008) Nanomedicine: design and application of magnetic nanomaterials, nanosensors and nanosystems. Wiley, Chichester

40. Nagawaka M, Oda H, Kobayashi K (2010) Inorganic and metallic nanotubular materials: recent technologies. Springer, Berlin
41. Leonhardt A et al (2003) Synthesis and properties of filled carbon nanotubes. Diam Relat Mater 12:790–793
42. Watts PCP et al (2002) Fe-filled carbon nanotubes: nano-electromagnetic inductors. Chem Mater 14:4505–4508
43. Kozhuharova R et al (2003) Synthesis and characterization of aligned Fe-filled carbon nanotubes on silicon substrates. J Mater Sci Mater Electron 14:789–791
44. Korneva G et al (2005) Carbon nanotubes loaded with magnetic particles. Nano Lett 5:879–884
45. Pal S, Chandra S, Phan MH, Mukherjee P, Srikanth H (2009) Carbon nanostraws: nanotubes filled with superparamagnetic nanoparticles. Nanotechnology 20:485604–485611
46. Yen JH et al (2005) Effect of nanowire catalyst for carbon nanotubes growth by ICP-CVD. Diam Relat Mater 14:841–845
47. Liu LF (2006) Template synthesis, characterization and magnetic property of Fe nanowires-filled amorphous carbon nanotubes array J. Phys D Appl Phys 39:3939–3944